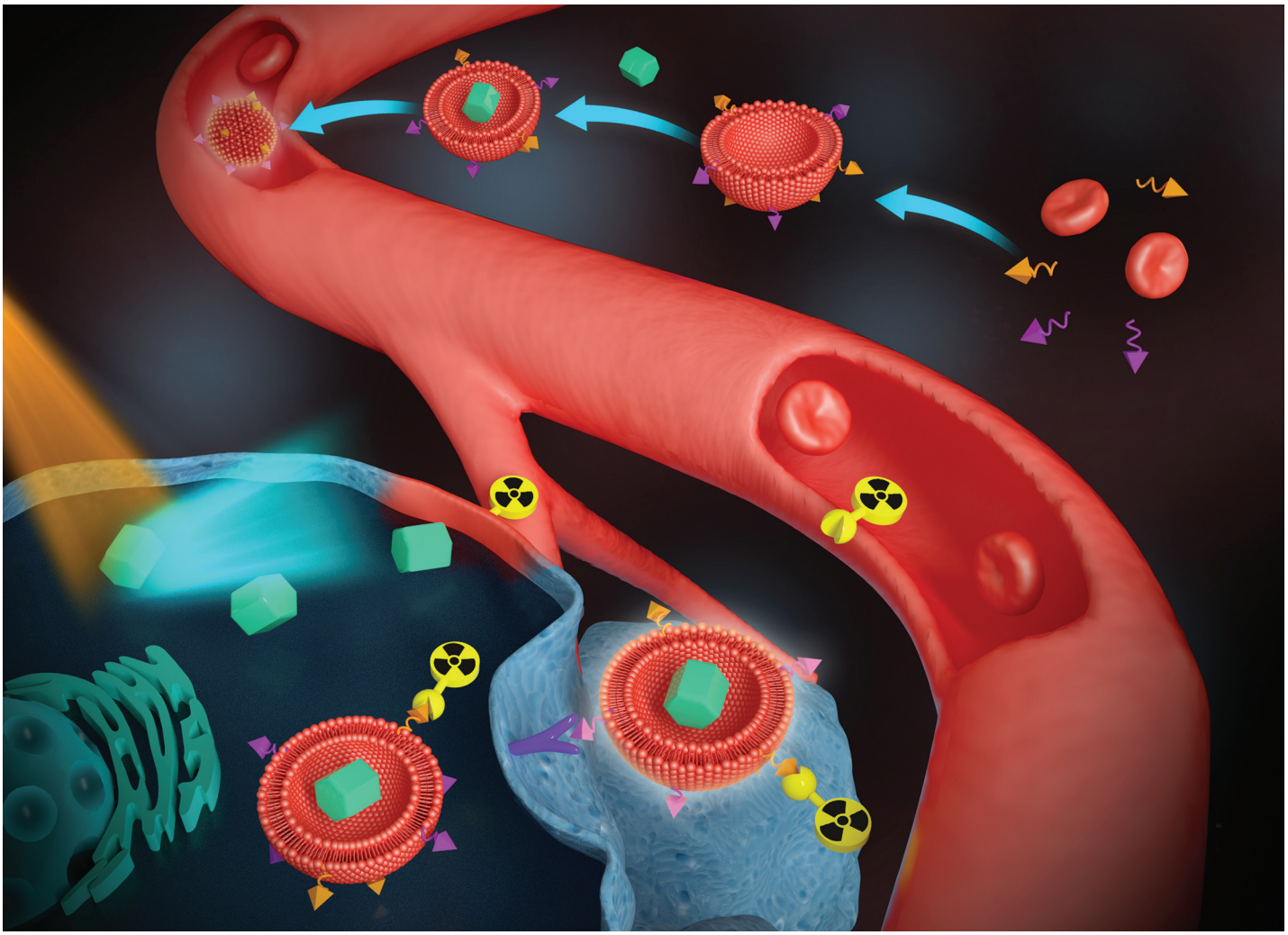

Highlighting research from Prof. Xiaoli Lan's research group at Union Hospital, Tongji Medical College, Huazhong University of Science and Technology.

Red blood cell membrane-coated upconversion nanoparticles for pretargeted multimodality imaging of triple-negative breast cancer

This authors introduce a multimodality molecular imaging platform by red blood cell membrane-coated upconversion nanoparticles, these biomimetic nanoparticles possess good biocompatibility and tumor targeting ability, providing a new potential biomedical application for early tumor imaging.

As featured in:

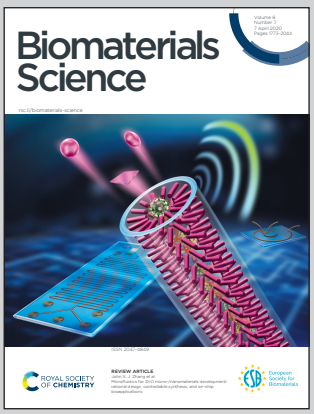

See Xiaoli Lan *et al.*, *Biomater. Sci.*, 2020, **8**, 1802.

ROYAL SOCIETY OF CHEMISTRY

rsc.li/biomaterials-science

Registered charity number: 207890

Biomaterials Science

ROYAL SOCIETY OF CHEMISTRY

PAPER

View Article Online
View Journal | View Issue

Cite this: *Biomater. Sci.*, 2020, **8**, 1802

Red blood cell membrane-coated upconversion nanoparticles for pretargeted multimodality imaging of triple-negative breast cancer†

Mengting Li,‡[a,b] Hanyi Fang,‡[a,b] Qingyao Liu,‡[a,b] Yongkang Gai,[a,b] Lujie Yuan,[a,b] Sheng Wang,[c] Huiling Li,[a,b] Yi Hou,[d] Mingyuan Gao [e] and Xiaoli Lan *[a,b]

Upconversion nanoparticles (UCNPs) have been widely employed for tumor imaging using magnetic resonance imaging (MRI) and upconversion luminescence (UCL) imaging. The short blood clearance time and immunogenicity of UCNPs have limited their further application *in vivo*. We have designed UCNPs camouflaged with an exterior red blood cell (RBC) membrane coating (RBC-UCNPs) to solve these problems. Moreover, because of some intrinsic disadvantages of MRI and UCL imaging, we investigated the use of pretargeted RBC-UCNPs for positron-emission tomography (PET) imaging to obtain more comprehensive information. Our data showed that RBC-UCNPs retained the immunity feature from the source cells and the superior optical and chemical features from the pristine UCNP cores. The tumor-targeting ability of RBC-UCNPs was enhanced by binding 1,2-distearoyl-*sn*-glycero-3-phosphoethanolamine-*N*-[folate(polyethylene glycol)-2000] (DSPE-PEG-FA) molecules onto the cell membranes. PET imaging with short half-life radionuclides to visualize the RBC-UCNPs was successfully realized by a combination of pre-targeting and *in vivo* click chemistry. Blood chemistry, hematology, and histologic analysis suggested good *in vivo* biocompatibility of the RBC-UCNPs. Our method provides a new potential biomedical application of biomimetic nanoparticles.

Received 6th January 2020,
Accepted 23rd February 2020

DOI: 10.1039/d0bm00029a

rsc.li/biomaterials-science

1. Introduction

Cancer remains a global public health problem.[1] Sensitive and specific tumor imaging holds great importance in its early detection and also in metastasis management.[2,3] A variety of modalities have been explored for the visualization, characterization, and measurement of neoplasms, including positron-emission tomography (PET), magnetic resonance imaging (MRI), computed tomography (CT), photoacoustic tomography (PAT), and optical imaging.[4] Upconversion nanoparticles (UCNPs), particularly lanthanide-doped nanocrystals, which convert near-infrared (NIR) radiation to visible light by a process called "upconversion luminescence" (UCL), are a promising new generation of fluorescent probes.[5–12] Compared with conventional down-conversion fluorescent agents, such as fluorescent dyes and quantum dots, UCNPs have unique chemical and optical properties such as the absence of autofluorescence, non-blinking, excellent photostability, narrow emission peaks, low toxicity, and low photo-damage to living systems, which further support their application in cancer diagnostics and imaging.[13–18] Because different imaging techniques have their own advantages and disadvantages, multimodality imaging strategies have the potential to harness the advantages of each modality to yield complementary and confirmatory information.

To date, nanotechnology has been widely applied in diagnosis (*e.g.*, molecular imaging) and therapy (*e.g.*, drug delivery).[19] However, when synthetic nanoparticles are introduced to *in vivo* applications and are exposed to body fluids, they are easily considered as intruders by the innate immune system, and rapidly recognized and eliminated by the reticuloendothelial system (RES)/mononuclear phagocyte system (MPS).[20–23] When nanoparticles are exposed to body fluids, nonspecific

[a]*Department of Nuclear Medicine, Union Hospital, Tongji Medical College, Huazhong University of Science and Technology, Wuhan 430022, China. E-mail: xiaoli_lan@hust.edu.cn; Fax: +86-27-83692633; Tel: +86-13886193262*
[b]*Hubei Province Key Laboratory of Molecular Imaging, Wuhan 430022, China*
[c]*School of Pharmacy, Tongji Medical College, Huazhong University of Science and Technology, Wuhan 430030, China*
[d]*Key Laboratory of Colloid, Interface and Chemical Thermodynamics, Institute of Chemistry, Chinese Academy of Sciences, Bei Yi Jie 2, Zhong Guan Cun, Beijing 100190, China*
[e]*Center for Molecular Imaging and Nuclear Medicine, State Key Laboratory of Radiation Medicine and Protection, School for Radiological and Interdisciplinary Sciences (RAD-X), Soochow University, Suzhou 215123, China*

†Electronic supplementary information (ESI) available. See DOI: 10.1039/d0bm00029a

‡These authors contributed equally to this work.

proteins and biological molecules bind to their surface, inducing the formation of a protein ring (protein corona) structure,[24] which interferes with the interaction between nanoparticles and biological systems and accelerates the pace of nanoparticle clearance by the immune system. Hence, a critical issue for successful nanoparticle-based biomedical application is reducing the RES/MPS uptake. For this purpose, one classical approach is the surface functionalization of nanoparticles with polymer materials (*e.g.*, polyethylene glycol (PEG), polyvinylpyrrolidone (PVP), and polychlorinated biphenyl (PCB)).[24–33] Among many polymer materials, PEG can reduce the adsorption of nonspecific proteins to a certain extent and inhibit flocculation, opsin action, and subsequent complement activation. PEG is currently the most commonly used nanoparticle surface modification material.[34] However, toxicity studies have shown that PEG may cause blood clotting and cell agglutination.[35] In addition, with the widespread application of PEG in food and cosmetics, investigations have shown that 22%–25% of healthy blood donors carry PEG antibodies.[36] As a result, many patients will experience accelerated clearance after the systemic administration of drugs containing PEG. These polymer materials either still interact with certain biomolecules or motivate the activation of anti-PEG immunological responses to different degrees, known as the "accelerated blood clearance" phenomenon.[27,35,37,38] Thus, concerns still exist over the validity and safety of using synthetic polymer materials to extend the application of UCNPs.

The cell is the basic structural, functional, and biological unit of organisms. As a safer and more biocompatible vector, the use of natural cellular membranes for nanoparticle surface functionalization has become a focus of research. By coating the surface of nanoparticles with cell membranes, the nanoparticles can inherit complex and unique surface physicochemical properties from the source cells.[39] This top-down approach of directly binding the cell membrane to the nanoparticles not only reduces the adsorption of nonspecific proteins, but also makes the preparation process relatively straightforward.[40] Red blood cells (RBCs) have a lifespan of up to 120 days.[25] As nature's long-circulating delivery vehicle, the surface of RBCs is composed of numerous "self-marker" proteins (*e.g.*, CD47), glycans, and acidic sialic acid moieties, which effectively prevent immune attack.[41–43] As stealth coating materials, the surface antigenic diversity of RBCs completely replicates onto the nanoparticle surface with proper orientation (*i.e.*, right-side-out).[40]

Inspired by the RBC membrane camouflage strategy, we hypothesize that RBC-derived membrane coated UCNPs (RBC-UCNPs and FA-RBC-UCNPs) can be used for the targeted multimodality imaging of 4T1 breast cancer, a triple-negative breast cancer (Fig. 1). In this study, cell membranes were collected from RBCs, reconstructed into vesicles (RBC-vesicles), and then coated onto UCNPs. We demonstrated that the obtained RBC-UCNPs exhibit extended blood circulation time and reduced uptake by the RES. Subsequently, a cancer-targeting molecule, 1,2-distearoyl-*sn*-glycero-3-phosphoethanolamine-*N*-[folate(polyethylene glycol)-2000] (DSPE-PEG-FA) was inserted into the phospholipid bilayer of cell membranes to investigate the tumor-targeting ability of the biomimetic nanoparticles. Benefiting from the inhibition of protein interaction, the tumor-targeting efficiency of cell membrane-coated nanoparticles was significantly improved. The UCNP core is visible on MRI and can convert near-infrared radiation to visible light. Considering their rapid and highly selective nature, click chemistry plays a significant role in a range of radiopharmaceutical community and biological applications. Furthermore, reports have begun to emerge in an *in vivo* application to facilitate a novel pre-targeting strategy for the imaging and therapy of cancer. The implementation of this successful approach in nuclear imaging could lead to exciting improvements in image quality and reduced radiation dose to non-target organs and

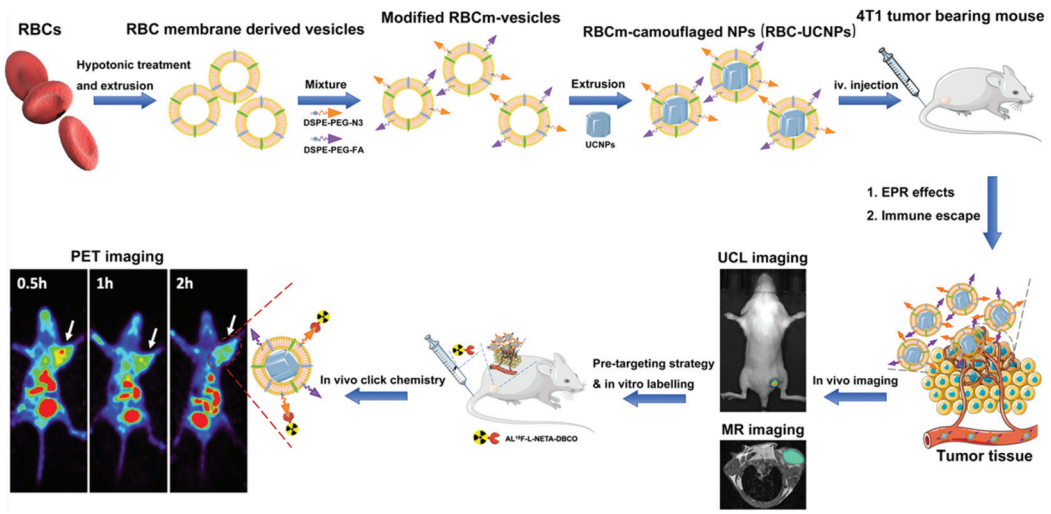

Fig. 1 The schematic of the preparation process of the modified RBC-UCNPs and their applications of MRI, UCL imaging and PET imaging in triple-negative breast cancer bearing mice.

tissues.[44] The coated cell membrane can be modified for radionuclide imaging by a combination of pre-targeting methods with *in vivo* click chemistry; this novel biomimetic nano-platform was further investigated for efficient multimodality tumor imaging. Lastly, the *in vivo* toxicity evaluation results showed the favorable biocompatibility of our biomimetic nanoparticles.

2. Materials and methods

2.1. Materials and reagents

Phosphate-buffered saline (PBS; 1×, 0.0067 M PO_4^{3+}), RPMI 1640 media, trypsin, ethylenediaminetetraacetic acid (EDTA), and penicillin–streptomycin were obtained from ThermoFisher (USA). Fetal bovine serum (FBS) was purchased from Sciencell (USA). 4′,6-Diamidino-2-phenylindole (DAPI), 4% paraformaldehyde, and Cell Counting Kit-8 (CCK-8) were purchased from Boster (Wuhan, China). Phospholipids with various functionalized head-groups including DSPE-PEG-FA, 1,2-distearoyl-*sn-glycero*-3-phosphoethanolamine-*N*-[azido (polyethylene glycol)-2000] (DSPE-PEG-N_3) and DBCO were obtained from Nanocs (USA) and Avanti Polar Lipids (USA). All the aqueous solutions were prepared by using purified deionized water purified on an experimental water purification system (Super series, Easy ultra-pure Water System, Heal Force, China). The other solvents and reagents used in this work were obtained from Aladdin-Reagent (China) and Sinopharm Chemical Reagent (China). Culture flasks and culture plates (12-well and 96-well) were purchased from Corning (USA).

2.2. Cell culture

4T1 tumor cells were purchased from American Type Culture Collection (ATCC) and cultured in the standard cell medium recommended by American Type Culture Collection, at 37 °C in a humidified atmosphere containing 5% CO_2.

2.3. Synthesizing the $NaGdF_4$:Yb,Tm nanoparticles

See the ESI.†

2.4. Preparation of RBC membrane-derived vesicles (RBC-vesicles)

The vesicles derived from RBC membranes were prepared according to a recent report with modifications.[25,27] BALB/c mice were chosen to collect natural RBCs to prepare the RBC membranes. All the animal procedures complied with the guidelines of the Institutional Animal Care and Use Committee at Huazhong University of Science and Technology. Fresh whole blood was withdrawn from the orbit of BALB/c mice (male, 6–8 weeks old) with 1.5 mg of EDTA per mL of blood for anticoagulation. The blood was centrifuged at 3000 rpm for 20 min at 4 °C to collect the erythrocytes. The resultant RBCs were washed with ice-cold 1× PBS three times and recollected by centrifugation (800*g* for 5 min at 4 °C) to remove the plasma. The RBC ghosts were obtained *via* a hypotonic treatment by mixing washed RBCs with 1/4× PBS (PBS/deionized water = 1 : 3) for 2 h at 4 °C, during which hemoglobin was released. This was centrifuged at 15 000 rpm for 5 min at 4 °C to collect RBC ghosts and remove the intracellular components of RBCs. Then, the RBC membrane-derived vesicles were prepared from the obtained RBC ghosts by subsequent extrusions. Briefly, the obtained RBC ghosts were gently sonicated using a bath sonicator (53 kHz, 100 W, 5 min) and were subsequently extruded through 400 nm polycarbonate porous membranes with a mini extruder (Avanti Polar Lipids, USA). The resultant RBC membrane-derived vesicles were stored in PBS at 4 °C before use. Characterization of the RBC membranes is described in the ESI.†

2.5. Preparation and characterization of RBC-UCNPs

To encapsulate UCNPs into RBC vesicles, 400 μl of 500 μL mL^{-1} RBC vesicles were first mixed with 1 mg of $NaGdF_4$:Yb, Tm UCNPs in 1 mL of PBS and sonicated for 30 s (53 kHz, 100 W). Subsequently, the mixture was repeatedly extruded through a 400 nm polycarbonate porous membrane 11 times on a mini-extruder, and then excess RBC membrane-derived vesicles were removed by centrifugation (1000*g* for 10 min at 4 °C). The resultant RBCm-UCNPs were stored in 1× PBS at 4 °C for further use. Dynamic light scattering (DLS; Nano-Zen 3600, Malvern Instruments, UK) was used to measure the hydrodynamic diameter and zeta potential at room temperature. The morphology of UCNPs and RBC-UCNPs was characterized by using a transmission electron microscope (TEM; JEM-2010 ES500 W, Japan) operating at 200 keV. The samples were prepared by contacting the UCNP and RBC-UCNP suspension droplets with copper grids for 1 min and then negatively stained with 1% uranyl acetate and 1% phosphotungstic acid for 30 s before the TEM characterization. UV-vis spectrometry (Synergy 2, BioTek Instruments Inc., USA) was used to characterize the absorption properties of samples. Protein characterization was conducted by using the sodium dodecyl sulfate-polyacrylamide gel electrophoresis (SDS-PAGE) method reported previously.[45] The RBC lysate, RBC-vesicles, and purified RBC-UCNPs were added into SDS buffer as measured by the BCA assay kit. The samples were heated at 90 °C for 10 min and 20 μL of each sample was loaded into each well in a 10% SDS-polyacrylamide gel. Samples were run at 100 V for 2 h and the obtained gel was stained with Coomassie blue, washed with deionized water, and then imaged.

2.6. Preparation and characterization of FA-RBC-UCNPs

RBC membrane-derived vesicles were obtained from 1 mL of blood as described previously and then incubated with 50 μg of DSPE-PEG-FA at 37 °C for 30 min to form FA-PEG-DSPE-RBCs.[46] All samples were centrifuged at 1000*g* for 10 min and then washed with PBS three times before further use. The FA-modified RBC membranes were reconstructed into vesicles and then coated onto UCNPs as described previously. DLS and SDS-PAGE were also conducted to analyze the differences in physical characteristics and biological properties before and after surface modification in hydrodynamic size, zeta potential, and protein content. To

confirm that the coating of DSPE-PEG-FA onto the UCNPs did not significantly influence the original UCNP optical properties, the spectra of RBC-UCNPs and FA-RBC-UCNPs were characterized with an external 980 nm laser device (FLS 980, Edinburgh Instruments Ltd, UK).

2.7. Cell cytotoxicity assay

The 4T1 breast cancer cells were seeded in 96-well plates at a density of 1×10^4 cells per well and cultured for 12 h. UCNPs, RBC-UCNPs, or FA-RBC-UCNPs at various concentrations (*i.e.*, 1, 2, 5, 25, 100 and 500 μg mL^{-1}) were added to the medium, and then the cells were incubated for another 24 h or 48 h. In the control group, the cells were grown without any particles. At the end of the incubation, 5 mg mL^{-1} CCK-8 PBS solution was added and continued to incubate for another 2 h. Finally, the absorbance values of the cells per well were measured with a microplate reader (iMark™ Microplate Absorbance Reader, Bio-Rad, USA) at 450 nm for analyzing the cell viability. The background absorbance of the well plate was measured and subtracted. The cytotoxicity was calculated by the optical density (OD) values of treated groups (T) divided by the OD values of the control group (C) ($T/C \times 100\%$).

2.8. Animal models

BALB/c mice (female, 6–8 weeks old) were purchased from Hubei Provence Center for Disease Control and Prevention (Wuhan, China). Animals received care under specific pathogen-free conditions, within facilities approved by the Laboratory Animal Care of Huazhong University of Science and Technology, and in compliance with the regulations and standards of the Institutional Animal Care and Use Committee of Tongji Medical College of Huazhong University of Science and Technology. 4T1 breast tumor grafts were performed by subcutaneous (s.c.) injection of 80 μL of serum-free cell medium containing 1×10^7 4T1 cells into the right front leg of each mouse. After the tumor volume reached approximately 50 mm^3, the tumor-bearing mice were used for further experiments.

2.9. *In vivo* UCL imaging

For *in vivo* UCL imaging, 12 BALB/c mice bearing 4T1 tumor grafts (n = 3 per group) received i.v. injection of 200 μL of PBS or PBS containing nanoparticles with different surface features (*i.e.*, UCNPs, RBC-UCNPs, and FA-RBC-UCNPs) at a concentration of 5 mg mL^{-1}. At various time points after the injection (*i.e.*, 3, 6, 12, 24, 36 and 48 h), all mice were anesthetized with 2% isoflurane, and then *in vivo* UCL imaging was conducted by using a modified *in vivo* imaging system (IVIS Lumina XRMS, Caliper, USA) equipped with fluorescent filter sets (excitation/emission = 980/535 nm). The images obtained before the injection of various samples were regarded as control images. The laser power used in the mice experiment was set as 30 W and the field of view was 12.5 cm in diameter. The images were acquired for 30 s and further analyzed with Living Image Software (PerkinElmer, USA).

2.10. *In vivo* magnetic resonance imaging

12 BALB/c mice bearing 4T1 tumor grafts (n = 3 per group) received an i.v. injection of 200 μL of PBS containing various nanoparticles (*i.e.*, UCNPs, RBC-UCNPs, or FA-RBC-UCNPs) or Gd-DTPA solutions. The dose level for UCNPs, RBC-UCNPs, FA-RBC-UCNPs, and Gd-DTPA was set as 15 mg of Gd per kilogram body weight in all imaging experiments. MR images were acquired on a 7.0 T animal MRI instrument (BioSpec 70/20 USR, Bruker, USA) at 24 h after the injection of nanoparticles and 10 min after the injection of Gd-DTPA at 24 h post-injection. The detailed imaging parameters were set as follows: field of view (FOV) = 3.5 × 4.5 cm^2; matrix size = 128 × 128; slice thickness = 1 mm; echo time (T_E) = 11 ms; repetition time (T_R) = 90, 150, 300, 500, 800, 1200, 2000, and 3000 ms; number of excitation (NEX) = 4. $T1$ maps were calculated by the pixel-wise fitting of the TR-dependent signal intensity changes to a single-exponential function. The mice were anesthetized with 2% isoflurane delivered *via* a nose cone during the imaging sessions.

2.11. Pre-targeting injection of DSPE-PEG-N_3 modified RBC-UCNPs or FA-RBC-UCNPs

DSPE-PEG-N_3 was incubated with RBC-vesicles for 30 min at 37 °C to form N_3-PEG-DSPE-RBCm. DSPE-PEG-FA and DSPE-PEG-N_3 were both incubated with empty RBC membranes for 30 min at 37 °C to form N_3(FA)-PEG-DSPE-RBC membranes. All samples were centrifuged at 1000*g* for 10 min before further use. The DSPE-PEG-modified RBC membranes were reconstructed into vesicles and then coated onto UCNPs as described previously. N_3(FA)-RBC-UCNPs and N_3-RBC-UCNPs were intravenously injected into the 4T1 subcutaneous tumor-bearing mice by pre-positioning for 36 h.

2.12. Synthesis of $Al^{18}F$-NETA-L-DBCO

Stock solutions were prepared, including 0.4 M $KHCO_3$ (for eluting), metal-free glacial acetic acid, 2 mM $AlCl_3$ in 0.1 M sodium acetate buffer and NaOAc (0.1 M pH = 4). Preconditioning of the Sep-Pak Light Accell Plus QMA cartridge was performed by eluting with 0.4 M $KHCO_3$ (10 mL) then water (15 mL). ^{18}F (100 mCi) was loaded into the cartridge and washed with water (5 mL). The cartridge was eluted with 1 mL of saline to obtain ^{18}F solution in saline, 50 μL per tube. The hottest fraction was used for labeling. (Usually, the third or the fourth one was the largest one.) 5 μL of $AlCl_3$ solution (10 nmol) was added to ^{18}F solution, and the pH was adjusted to 4 by adding glacial acetic acid (~3 μL). The resulting mixture was incubated at room temperature for 10 min. The chelator (DBCO-L-NETA) solution (10 μL, 20 nmol) and 10 nmol buffer solution were added. The mixture was incubated in a 100 °C heating block for 15 min. The preconditioning of the Sep-Pak Light C-18 cartridge was performed with 10 mL of 95% ethanol and 10 mL of DI water. The solution was cooled to room temperature, the product was pushed into the column, and 5 ml of water and 0.5 ml of anhydrous

ethanol were used to wash the column. Then the product ($Al^{18}F$-NETA-L-DBCO) was collected.

2.13. Micro PET/CT imaging and biodistribution study

After the *in vitro* labeling of $Al^{18}F$-NETA-L-DBCO was completed, the mice bearing 4T1 tumor grafts (n = 3 per group) were injected *via* the tail vein for click chemistry *in vivo*. At 0.5, 1, and 2 h after the injection of $Al^{18}F$-NETA-L-DBCO, mice were anesthetized with 2% isoflurane and micro PET/CT static imaging was performed. Mice were placed in the supine position, and static images were collected for 10 min using a small-animal PET/CT scanner (BioCaliburn LH, Raycan Technology Co., Ltd, Suzhou, China). PET images were reconstructed with the ordered-subset expectation maximization three-dimensional/maximum *a posteriori* probability algorithm, and then the analysis of images was done using Amide (http://amide.sourceforge.net) and OsiriX (Osirix, Geneva, Switzerland) software.

For the biodistribution study, at 0.5, 1 and 2 h after $Al^{18}F$-NETA-L-DBCO injection, the 4T1 (n = 5 per group) mice were sacrificed, and the biological samples of interest (*e.g.*, blood, brain, heart, lungs, liver, spleen, kidneys, stomach, small intestine, large intestine, muscle, bones, and tumor) were collected. Tissues were washed and weighed, and all tissues were counted with an automatic well-type gamma counter (2470 Automatic Gamma Counter WIZARD, PerkinElmer, Norwalk CT, USA). Organ and tissue uptakes were expressed as a percentage of the injected dose per gram of tissue mass (% ID g^{-1}) and corrected for radioactive decay.

2.14. *In vivo* toxicity evaluation

24 BALB/c mice (n = 6 per group) received an i.v. injection of 200 μL of PBS, or PBS containing UCNPs, RBC-UCNPs or FA-RBC-UCNPs at the concentration of 5 mg mL^{-1}. The general status of the mice was evaluated every day and body weights were measured using a digital scale every three days. All mice were euthanized on the 30th day after the injection and their blood samples and major organs (*i.e.*, hearts, livers, spleens, lungs and kidneys) were collected. Alanine aminotransferase (ALT), aspartate aminotransferase (AST), and alkaline phosphatase (ALP), blood urea nitrogen (BUN), and creatinine (CRE) were measured with a blood biochemical autoanalyzer (Chemray 240, Rayto Life and Analytical Sciences Co., Ltd, China). White blood cell count, red blood cell count, hemoglobin, hematocrit, mean corpuscular volume, mean corpuscular hemoglobin, mean corpuscular hemoglobin concentration, platelets, and red blood cell distribution width were also measured. Parts of their organs were fixed in 4% neutral buffered formalin, paraffinized, and cut into 4 μm sections. Then these sections were stained with hematoxylin and eosin (H&E) and examined using an optical microscope (IX73, Olympus, Japan).

2.15. Statistical analysis

Statistical analysis was performed with the commercial software (GraphPad Prism 6.0 GraphPad Software™, La Jolla, CA, USA) to analyze the data of the biodistribution study. All data are expressed as mean ± standard deviation (SD). The differences between two groups were compared by Student's t-test (two-tailed) and were considered statistically significant when $P < 0.05$.

3. Results and discussion

3.1. Preparation and characterization of RBC-UCNPs

The preparation process of biomimetic RBC-UCNPs consisted of three steps: (1) preparing membrane-derived vesicles from natural RBCs, (2) synthesis of hydrophilic UCNPs, and (3) fusing the RBC-vesicles onto UCNPs. The RBC membrane-derived vesicles were prepared as recently reported.[22,24] Briefly, RBCs from the mouse blood were subjected to a hypotonic treatment to remove their intracellular components, which resulted in empty RBCs (*i.e.*, RBC ghosts) (Fig. S1, ESI†). After purification, the RBC ghosts were subsequently sonicated and extruded through 400 nm polycarbonate porous membranes on an extruder to produce RBC-vesicles. The resultant RBC-vesicles had a hydrodynamic diameter of around 400 nm and a zeta potential of −12.1 mV (Fig. S2†), which is consistent with recent reports.[22] Concurrently, the pristine $NaGdF_4$:Yb, Tm UCNPs were synthesized as described in previous papers. Finally, the mixture of RBC-vesicles and synthesized UCNPs was extruded through 400 nm polycarbonate porous membranes 11 times. The mechanical force induced by the extrusion process facilitated the encapsulation of the RBC-vesicles over the surface of UCNPs, forming the final biomimetic product RBC-UCNPs. The RBC-UCNPs were monitored for changes in size, zeta potential, particle morphology, protein content, and UV-vis absorption properties before and after the encapsulation process.

Dynamic light scattering was employed to characterize changes in the UCNPs before and after the cell membrane coating. The hydrodynamic diameter of UCNPs varied from 115.6 nm to 138.9 nm (Fig. 2a and b). This ~20 nm increase in diameter is in agreement with the reported thickness (approximately 8 nm) of two layers of cell membrane lipid bilayers.[47] Accordingly, the zeta potential changed to approximate that of RBC-vesicles (−12.1 mV) (Fig. 2c). The shift of surface charge is likely due to the charge screening effects caused by the RBC membrane coating, both indicating successful RBC membrane encapsulation of the UCNPs. Consistently, the transmission electron microscopy (TEM) images unequivocally showed the UCNP core of approximately 20 nm in diameter, and the spherical RBC-UCNPs with a characteristic core–shell structure as expected of approximately 30 nm in diameter (Fig. 2d–g). The outer lipid bilayer shell of approximately 8 nm is consistent with the reported RBC membrane thickness of 5–10 nm, indicating a successful contiguous membrane coating.

Following the structural studies, the protein content of RBC lysate, RBC-vesicles, and RBC-UCNPs was carried out in parallel using sodium dodecyl sulfate-polyacrylamide gel electrophoresis (SDS-PAGE). Compared with the RBC lysate, the cell

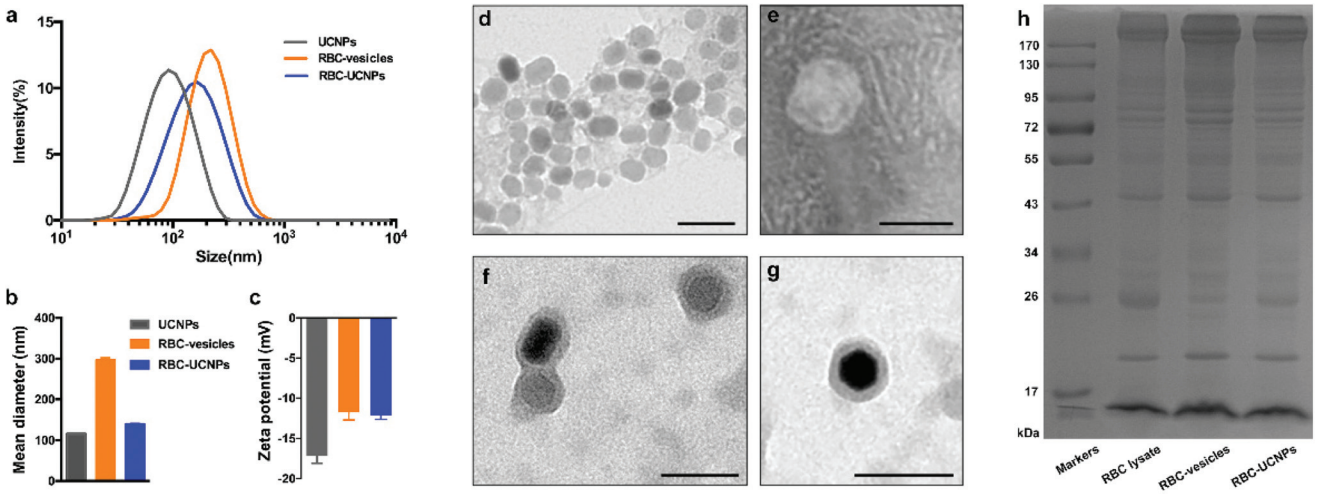

Fig. 2 Characteristics of UCNPs and RBC-UCNPs. (a) Size intensity curves of UCNP cores, RBC-vesicles, and RBC-UCNPs measured by dynamic light scattering (DLS). (b) Hydrodynamic size of UCNP cores, RBC-vesicles, and RBC-UCNPs. Bars represent means ± SD (n = 3). (c) Zeta potential of UCNP cores, RBC-vesicles, and RBC-UCNPs. Bars represent means ± SD (n = 3). Transmission electron micrographs (TEM) of (d) UCNP cores, (e) RBC-vesicles after extruding through 100 nm polycarbonate porous membranes, (f) multiple RBC-UCNPs, and (g) a RBC-UCNP. TEM samples were negatively stained with uranyl acetate. All scale bars = 50 nm. (h) SDS-PAGE protein identification photograph of RBC lysate, RBC-vesicles, and RBC-UCNPs.

membrane proteins were mostly retained in the form of RBC vesicles and the resulting RBC-UCNPs after the hypotonic and extruding processes (Fig. 2h), suggesting a successful translocation of the RBC membranes to the UCNPs' surface. UV-vis absorption spectra indicated that after the fusion process, RBC-UCNPs had gained an additional absorption of approximately 400 nm, which is in agreement with the characteristic absorption peak of RBC membrane-derived vesicles and is absent from the curve of the original UCNPs (Fig. S3†). Taken together, these results listed above revealed the successful translocation of RBC-vesicles onto UCNP surfaces with a correct membrane orientation and the preservation of most membrane proteins from the source RBCs.

We further tried to optimize the ratio between RBC membranes and UCNP cores during the fusing process. The result indicated that RBC-UCNPs displayed the smallest diameter when 1 mg of UCNPs was added to 200 μl of RBC-vesicles (Fig. S4†). In the following study, we therefore encapsulated RBC-vesicles and UCNPs in this ratio. The obtained RBC-UCNPs possessed excellent stability in 1× PBS over 7 d (Fig. S5†). The UCNPs showed strong green upconversion luminescence under 980 nm NIR irradiation, and the emission peaks agreed with the typical emission maximum at approximately 800 nm (Fig. S6†).[48] It was noteworthy that the RBC membrane coating barely affected the luminescence emission, which ensures its further use in *in vivo* tumor imaging experiments.

3.2. Preparation and characterization of FA-RBC-UCNPs

The folate receptor is a highly selective tumor marker overexpressed in various cancers.[49] Folic acid (FA), a high affinity ligand of the folate receptor, has been widely used for tumor targeting. FA molecules were inserted into the surface of the RBC-UCNPs to investigate the tumor-targeting ability of nanoparticles. Owing to the fluidity of lipid bilayer membranes, it is easy to obtain FA-modified RBC membranes by physically mixing empty RBCs with DSPE-PEG-FA at 37 °C. DLS and SDS-PAGE showed that unmodified and FA-modified RBC-UCNPs had similar physicochemical properties and protein content, correspondingly (Fig. 3a–c and Fig. S7†). These results revealed that the surface modification of DSPE-PEG-FA had no visual influences on the basic properties of RBC-UCNPs. After 980 nm NIR irradiation, no significant UCL intensity reduction of FA-RBC-UCNPs was noticed compared with UCNPs and RBC-UCNPs (Fig. 3d).

A CCK-8 assay was performed to evaluate the cytotoxicity of nanoparticles to 4T1 breast cancer cells. 4T1 breast cancer cells were co-incubated with UCNPs, RBC-UCNPs and FA-RBC-UCNPs at various concentrations (up to 500 μg mL^{-1}) for 24 h and 48 h. The results showed that the survival rate of cells in each group was >80% (Fig. 3e and f). UCNPs, RBC-UCNPs and FA-RBC-UCNPs had no obvious toxicity to 4T1 breast cancer cells. All results listed above provided a basis for these biomimetic nanoparticles to be tested *in vivo*.

3.3. Upconversion fluorescence imaging of tumors *in vivo*

To investigate the nanoparticles' optical properties *in vivo*, UCL imaging was performed before and at different time points after intravenously injecting 200 μL of PBS or PBS containing equal amounts of various nanoparticles into mice bearing 4T1 subcutaneously transplanted tumors. A set of true-color UCL images was acquired by using a modified small-animal imaging system. All mice were euthanized at

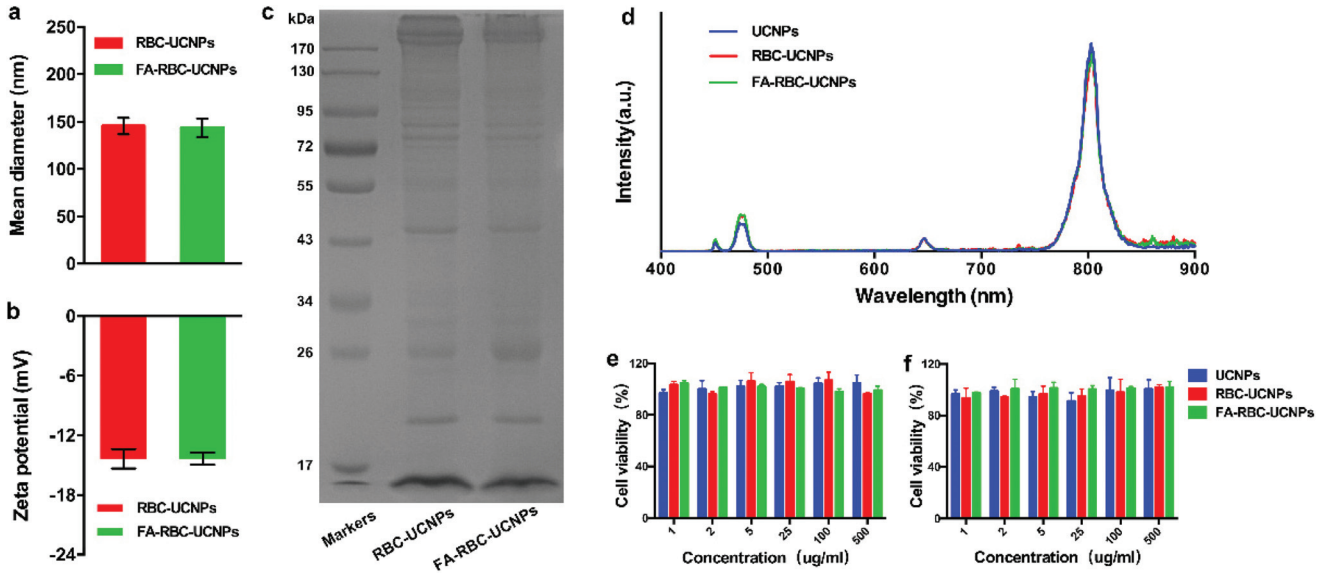

Fig. 3 Characteristics of UCNPs, RBC-UCNPs and FA-RBC-UCNPs. (a) Mean diameter, (b) zeta potential, (c) SDS-PAGE protein identification photograph, and (d) the upconversion emission spectrum of unmodified and modified RBC-UCNPs with DSPE-PEG-FA. 4T1 cell viability after 24 h (e) and 48 h (f) incubation with UCNPs, RBC-UCNPs and FA-RBC-UCNPs at different concentrations. Error bars: Standard deviations (n = 3).

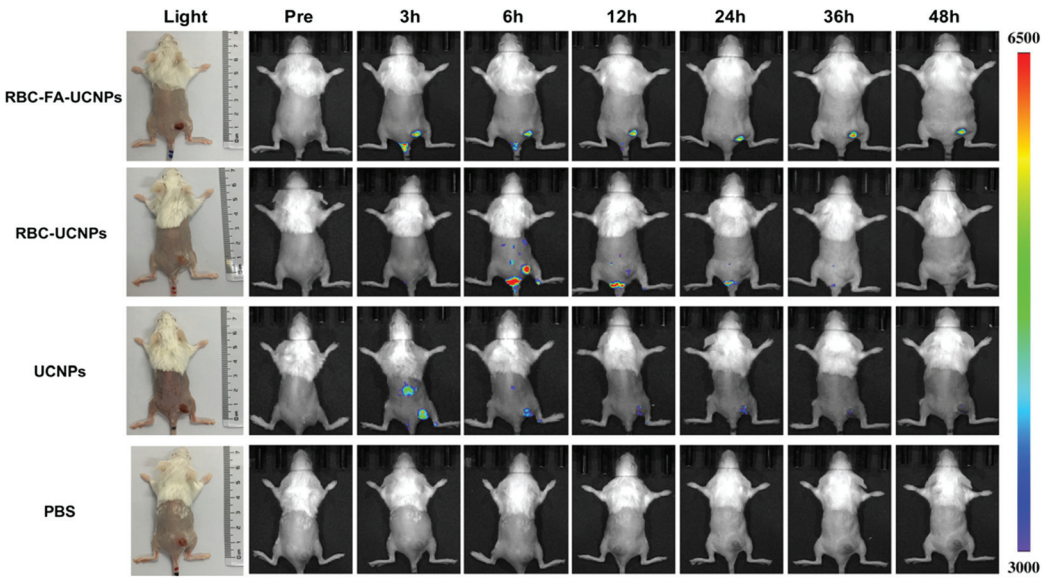

Fig. 4 Left panel: The white light photos of 4T1 tumor bearing Balb/c mice (tumor site: the flank region of the right hind leg). Right panel: Four sets of upconversion fluorescence images induced by the 980 nm laser beam were captured before and at different time points after intravenous injection of FA-RBC-UCNPs, RBC-UCNPs, UCNPs, and PBS, respectively. Mice injected with PBS were considered as the control group and placed in the last row.

48 h after the injection, then their major organs and tumors were harvested and used for *ex vivo* imaging.

From the pre-time points of the PBS group (Fig. 4, row 4) and each experimental group, when upconversion fluorescence imaging (980 nm excitation) was performed, there was no spontaneous fluorescence interference. For the UCNP group, due to the enhanced permeability and retention (EPR) effect, nanoparticles showed uptake by tumors to a certain extent (Fig. 4, row 3). However, they were quickly recognized by the RES (liver uptake is relatively higher). The tumor site's UCL signal was not visible at the later time points during the imaging process. Because the RBC-vesicle coating reduced the generation of a protein corona, the RBC-UCNP group had a significantly lower liver uptake (Fig. 4, row 2) compared with the UCNP group. The mice injected with FA-RBC-UCNPs showed the brightest UCL signal at the tumor site at all time points

compared with the other groups. The UCL optical signal could be observed at the tumor site 3 h after the samples' injection, and the signal lasted at least for 48 h, peaking at 36 h (Fig. 4, row 1). The quick accumulation and long-time retention of FA-RBC-UCNPs at the tumor site suggest the good targeting ability of these biomimetic nanoparticles to 4T1 tumor grafts.

3.4. MR imaging of tumors *in vivo*

To further investigate the feasibility of using biomimetic nanoparticles as high-performance MRI contrast agents, FA-RBC-vesicle or RBC-vesicle coated UCNPs were used to detect subcutaneously grafted 4T1 tumors *in vivo*. With reference to the UCL imaging results, *T*1-weighted MR images were acquired at 36 h post-injection. The mother particles (UCNPs) and Gd-DTPA were set as control groups and used at the same dose level with respect to the Gd concentration. The tumor site is color-coded to better show the contrast enhancing effects. In comparison with UCNPs, the RBC membrane-camouflaged nanoparticles slightly enhanced the signal in the tumor region, probably caused by the EPR and increased the circulation time of particles at the tumor site. The MR signal is significantly increased by the FA-RBC-UCNPs, characterized by shortened *T*1 values at the tumor sites (Fig. 5).

3.5. Pre-targeting strategy and click chemistry method mediating *in vivo* micro PET/CT imaging and the biodistribution study

PET imaging technology, which has the advantage of high sensitivity while providing tomographic data, plays a significant role in tumor diagnosis. The characteristics of PET imaging can make up for the deficiencies of UCL imaging in detecting deep tissues. Fluorine-18 (^{18}F) is the most popular radioiso-

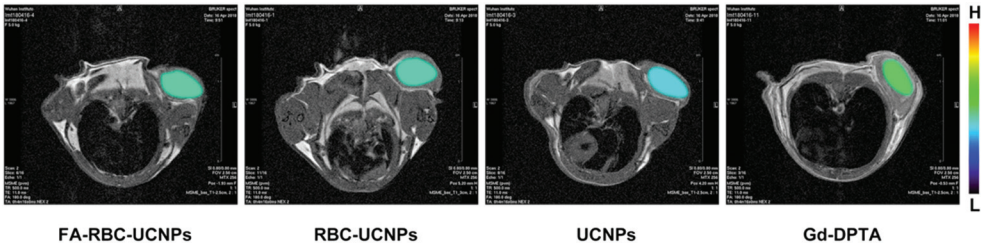

Fig. 5 *T*1-Weighted MR images of tumor-bearing mice acquired at 36 h after the intravenous injections of FA-RBC-UCNPs (column 1), RBC-UCNPs (column 2) or UCNPs (column 3) and 10 min of Gd-DTPA (column 4), respectively. The tumor site is color-coded to better show the contrast enhancing effects.

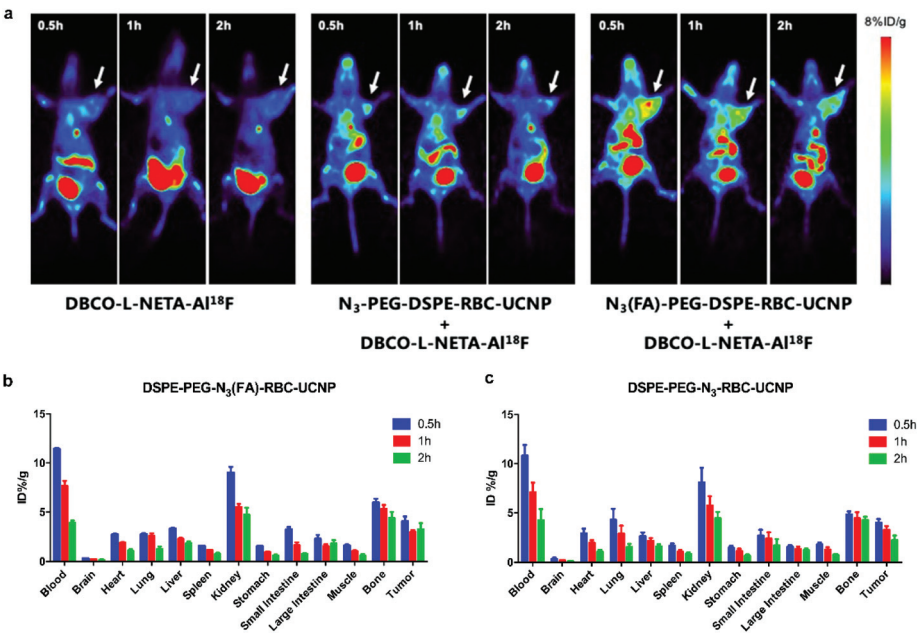

Fig. 6 PET imaging and bio-distribution study of 4T1 breast cancer bearing mice. (a) The tumor site (white arrows) showed the uptake of both the N_3-PEG-DSPE-RBC-UCNP group (middle panel) and N_3(FA)-PEG-DSPE-RBC-UCNP group (right panel), however, the chelator group (left panel, only injected DBCO-L-NETA-Al^{18}F) did not show an obvious radioactivity signal at the tumor site. Bio-distribution study of 4T1 breast cancer bearing mice (n = 5) at different time points in the N_3(FA)-PEG-DSPE-RBC-UCNP group (b) and N_3-PEG-DSPE-RBC-UCNP group (c).

tope investigated in PET imaging due to its excellent chemical, physical and nuclear properties, and can be acquired in almost all laboratories.[50] Therefore, the design of ^{18}F-based PET imaging will provide an important platform for the future *in vivo* applications of nanoparticles. ^{18}F's half-life is only 110 min, which does not match well with the metabolic characteristics of most nanoparticles *in vivo*. To use this short half-life radioisotope to monitor the *in vivo* distribution of the RBC membrane-camouflaged UCNPs, we chose a combination of a pre-targeting strategy and *in vivo* click chemistry. Our pre-targeting strategy involved the separate administration of tumor-targeted biomimetic nanoparticles and the radionuclide. After the tumor-binding nanoparticles were administered and had accumulated in the tumor, the radiolabeled probe Al^{18}F-NETA-L-DBCO, which has fast clearance properties, was administered to realize *in vivo* copper-free click chemistry.

DSPE-PEG-N_3 alone or with DSPE-PEG-FA were incubated with RBC-vesicles for 30 min at 37 °C to form N_3-PEG-DSPE-RBC and N_3(FA)-PEG-DSPE-RBC, respectively. All samples were centrifuged at 1000*g* for 10 min before further use. The DSPE-PEG-modified RBC membranes were reconstructed into vesicles and then coated onto UCNPs as described previously. N_3(FA)-PEG-DSPE-RBC-UCNPs (regarded as N_3(FA)-RBC-UCNPs) and N_3-PEG-DSPE-RBC-UCNPs (regarded as N_3-RBC-UCNPs) were intravenously injected into the 4T1 subcutaneous tumor-bearing mice 36 h before PET scanning. After the *in vitro* labeling of Al^{18}F-NETA-L-DBCO, the mice were also injected *via* the tail vein for click chemistry *in vivo* (Fig. S8†). Micro PET static imaging and biodistribution studies were performed at 0.5, 1, and 2 h after the injection of Al^{18}F-NETA-L-DBCO.

PET imaging results indicated that the N_3(FA)-RBC-UCNP group (Fig. 6a right panel) displayed a higher tumor uptake of the tracer compared with N_3-RBC-UCNPs (Fig. 6a middle panel). Both groups had a maximum tumor uptake at 30 min. However, the control group, only injected with Al^{18}F-NETA-L-DBCO, demonstrated no obvious imaging agent uptake at the tumor site in the whole imaging process (Fig. 6a left panel). In all three groups, the liver and spleen were not visible, but parts of the intestinal tract contained the tracer.

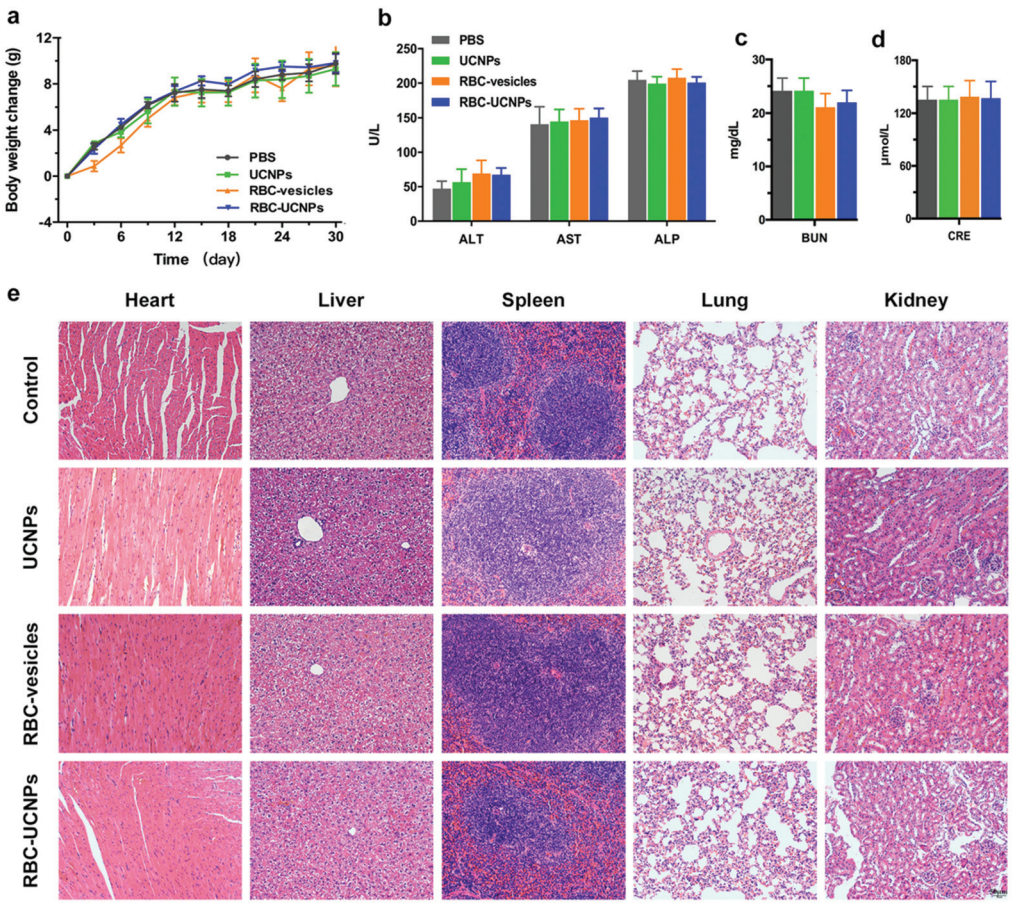

Fig. 7 *In vivo* toxicity evaluation by mice body weight measurement, blood test and histology analysis. (a) Mice body weight change curves over a span of 30 d after i.v. injection with PBS or PBS containing UCNPs, RBC-vesicles or RBC-UCNPs. Blood biochemistry data including liver function markers (b): ALT, AST and ALP and kidney function markers (c and d): BUN and CRE. Representative H&E staining images (e) of major organs from the euthanized mice on the 30th day after being i.v. injected with PBS or PBS containing UCNPs, RBC-vesicles or RBC-UCNPs. Magnification 20×, Bar = 50 μm. All error bars represent standard deviations (n = 6).

Quantitative analysis showed that since the unreacted radioactive probe was quickly cleared from the circulation, the blood concentration decreased rapidly with time in the N_3(FA)-RBC-UCNP and N_3-RBC-UCNP groups. The 30 min maximum tumor uptake indicated highly efficient click chemistry *in vivo* (Fig. 6b and c). Because the RES did not easily recognize these biomimetic nanoparticles, there were still many nanoparticles existing in the circulating blood at 36 h after injection, so the tumor to blood ratio (T/B) was relatively low. However, the T/B ratio remained stable or increased slightly over time (Fig. S9,† left), suggesting that the click-chemical response mediated by DBCO and N_3 was robust on the surface of the RBC membrane-camouflaged nanoparticles. The tumor-to-muscle ratio (T/M) of N_3(FA)-RBC-UCNPs was higher than that of N_3-RBC-UCNPs (Fig. S9,† right). All of the above results showed that we could successfully detect the biomimetic UCNPs at tumors sites based on the application of the short half-life radionuclide *via* a platform combining the pre-targeting strategy and *in vivo* click chemistry.

3.6 *In vivo* toxicity studies

The *in vivo* potential toxicity is always a considerable concern for nanomaterials used in biomedicine.[51] This is particularly vital for this kind of RBC membrane-camouflaged nanoparticles, as the mismatching of blood type sometimes may cause transfusion reactions and even death.[52] Herein, BALB/c mice (n = 6) received an i.v. injection of 200 μL of PBS, or PBS containing UCNPs or RBC-UCNPs at the concentration of 5 mg mL^{-1}, or PBS containing equivalent numbers of RBC-vesicles. Fluctuation in body weight is a direct indicator of a nanomaterial's *in vivo* toxicity. Neither death nor a significant difference in body weight between the control and treated groups was noted over a span of 30 days after the injection (Fig. 7a), which suggested that these particles had no overall *in vivo* side effects.

On the 30th day after the injection, all the mice were euthanized, and their blood and major organs (*i.e.*, hearts, livers, spleens, lungs, and kidneys) were collected for the blood test and H&E stained histology analysis. We observed no significant hepatic or renal toxicity induced by these nanoparticles, as indicated by normal values of liver function markers, including ALT, AST, and ALP (Fig. 7b) and kidney function markers, including BUN (Fig. 7c) and CRE (Fig. 7d). Also, the blood parameters of the treated groups remained normal compared with the control group (Table S1, ESI†). No obvious evidence of major organ damage was observed from the H&E stained sections (Fig. 7e).

All the above results suggested good biocompatibility of these RBC membrane-camouflaged nanoparticles, which indicated their suitability as a biomimetic nanoparticle platform for further clinical applications. Although more work is needed to systematically study the short- and long-term toxicity of these nanoparticles at various doses, our small-scale pilot toxicity study could promote further exploration of these biomimetic nanomaterials in biomedical applications.

4. Conclusions

In summary, we presented the successful encapsulation of UCNPs with RBC-membrane-derived vesicles. The resultant RBC-UCNPs exhibited excellent stealth properties, and MRI and UCL imaging abilities, which were inherited from natural RBCs and the pristine UCNP cores, respectively. Tumor-targeted RBC-UCNPs were obtained by inserting DSPE-PEG-FA into the cell membranes. The combination of a pre-targeting strategy and *in vivo* click chemistry successfully realized the 4T1 tumor PET imaging by short half-life nuclide-labeled biomimetic nanoparticles. Finally, *ex vivo* and *in vivo* toxicity studies demonstrated that no significant cytotoxicity or systemic toxicity was induced by the RBC-UCNPs.

In our study, the inserted FA was used to increase the tumor-targeting ability of RBC-UCNPs. However, we can extend our platform by inserting various DSPE-PEG functionalized head-groups to endow the RBC-UCNPs with more plentiful biological functions. On the basis of the combination of a pre-targeting strategy and click chemistry methodology, we creatively imaged the *in vivo* biodistribution of the biomimetic RBC-UCNPs at a specific time point by using a short half-life radionuclide. Hence, we can envision our platform for further applications by introducing other longer half-life nuclides or therapeutic nuclides to realize the early diagnosis and treatment of tumors, especially for deep-seated lesions. Our work provides a new angle of these biomimetic nanoparticles for biomedical applications and suggests that they will play an essential role in future imaging and treatment of diseases.

Abbreviations

ALP	Alkaline phosphatase
ALT	Alanine aminotransferase
AST	Aspartate aminotransferase
BUN	Blood urea nitrogen
CCK-8	Cell counting kit-8
CRE	Creatinine
CT	Computed tomography
DAPI	4′,6-Diamidino-2-phenylindole
DLS	Dynamic light scattering
DSPE-PEG-FA	1,2-Distearoyl-*sn-glycero*-3-phosphoethanolamine-*N*-[folate(polyethylene glycol)-2000]
DSPE-PEG-N_3	1,2-Distearoyl-*sn-glycero*-3-phosphoethanolamine-*N*-[azido(polyethylene glycol)-2000]
EDTA	Ethylenediaminetetraacetic acid
EPR	Enhanced permeability and retention
FA	Folic acid
FA-RBC-UCNPs	Folic acid modified red blood cell membrane-coated upconversion nanoparticles
FBS	Fetal bovine serum
H&E	Hematoxylin and eosin
MPS	Mononuclear phagocyte system
MRI	Magnetic resonance imaging
NIR	Near-infrared

OD	Optical density
PAT	Photoacoustic tomography
PBS	Phosphate-buffered saline
PCB	Polychlorinated biphenyl
PEG	Polyethylene glycol
PET	Positron emission tomography
PVP	Polyvinylpyrrolidone
RBC	Red blood cell
RBC-UCNPs	Red blood cell membrane-coated upconversion nanoparticles
RES	Reticuloendothelial system
SD	Standard deviation
SDS-PAGE	Sodium dodecyl sulfate-polyacrylamide gel electrophoresis
TEM	Transmission electron microscope
T/B	Tumor to blood
T/M	Tumor-to-muscle
UCL	Upconversion luminescence
UCNPs	Upconversion nanoparticles
% ID g^{-1}	Injected dose per gram

Conflicts of interest

The authors have declared that no competing interest exists.

Acknowledgements

This work was supported by the National Natural Science Foundation of China (No. 81630049 and No. 81501532).

References

1 R. L. Siegel, K. D. Miller and A. Jemal, Cancer statistics, *CA-Cancer J. Clin.*, 2016, **66**(1), 7–30.
2 A. C. Eifler and C. S. Thaxton, Nanoparticle therapeutics: FDA approval, clinical trials, regulatory pathways, and case study, *Methods Mol. Biol.*, 2011, **726**, 325–338.
3 R. Weissleder, Molecular imaging in cancer, *Science*, 2006, **312**(5777), 1168–1171.
4 R. Weissleder and M. J. Pittet, Imaging in the era of molecular oncology, *Nature*, 2008, **452**(7187), 580–589.
5 G. Tian, Z. Gu, L. Zhou, W. Yin, X. Liu, L. Yan, S. Jin, W. Ren, G. Xing, S. Li and Y. Zhao, Mn2+dopant-controlled synthesis of NaYF4:Yb/Er upconversion nanoparticles for in vivo imaging and drug delivery, *Adv. Mater.*, 2012, **24**(9), 1226–1231.
6 G. Chen, H. Qiu, P. N. Prasad and X. Chen, Upconversion nanoparticles: design, nanochemistry, and applications in theranostics, *Chem. Rev.*, 2014, **114**(10), 5161–5214.
7 R. Qiao, C. Liu, M. Liu, H. Hu, C. Liu, Y. Hou, K. Wu, Y. Lin, J. Liang and M. Gao, Ultrasensitive in vivo detection of primary gastric tumor and lymphatic metastasis using upconversion nanoparticles, *ACS Nano*, 2015, **9**(2), 2120–2129.
8 X. Chen, D. Peng, Q. Ju and F. Wang, Photon upconversion in core-shell nanoparticles, *Chem. Soc. Rev.*, 2015, **44**(6), 1318–1330.
9 G. Tian, X. Zhang, Z. Gu and Y. Zhao, Recent Advances in Upconversion Nanoparticles-Based Multifunctional Nanocomposites for Combined Cancer Therapy, *Adv. Mater.*, 2015, **27**(47), 7692–7712.
10 E. L. Guryev, N. O. Volodina, N. Y. Shilyagina, S. V. Gudkov, I. V. Balalaeva, A. B. Volovetskiy, A. V. Lyubeshkin, A. V. Sen', S. A. Ermilov, V. A. Vodeneev, R. V. Petrov, A. V. Zvyagin, Z. I. Alferov and S. M. Deyev, Radioactive ((90)Y) upconversion nanoparticles conjugated with recombinant targeted toxin for synergistic nanotheranostics of cancer, *Proc. Natl. Acad. Sci. U. S. A.*, 2018, **115**(39), 9690–9695.
11 S. M. Dong, J. T. Xu, T. Jia, M. S. Xu, C. N. Zhong, G. X. Yang, J. R. Li, D. Yang, F. He, S. L. Gai, P. P. Yang and J. Lin, Upconversion-mediated $ZnFe_2O_4$ nanoplatform for NIR-enhanced chemodynamic and photodynamic therapy, *Chem. Sci.*, 2019, **10**(15), 4259–4271.
12 Q. Q. Sun, F. He, C. Q. Sun, X. X. Wang, C. X. Li, J. T. Xu, D. Yang, H. T. Bi, S. L. Gai and P. P. Yang, Honeycomb-satellite structured pH/H_2O_2-responsive degradable nanoplatform for efficient photodynamic therapy and multimodal imaging, *ACS Appl. Mater. Interfaces*, 2018, **10**(40), 33901–33912.
13 F. Wang, R. Deng, J. Wang, Q. Wang, Y. Han, H. Zhu, X. Chen and X. Liu, Tuning upconversion through energy migration in core-shell nanoparticles, *Nat. Mater.*, 2011, **10**(12), 968–973.
14 L. Cheng, K. Yang, Y. Li, J. Chen, C. Wang, M. Shao, S. T. Lee and Z. Liu, Facile preparation of multifunctional upconversion nanoprobes for multimodal imaging and dual-targeted photothermal therapy, *Angew. Chem., Int. Ed.*, 2011, **50**(32), 7385–7390.
15 G. Chen and G. Han, Theranostic upconversion nanoparticles (I), *Theranostics*, 2013, **3**(4), 289–291.
16 D. Yang, Y. Dai, J. Liu, Y. Zhou, Y. Chen, C. Li, P. Ma and J. Lin, Ultra-small BaGdF5-based upconversion nanoparticles as drug carriers and multimodal imaging probes, *Biomaterials*, 2014, **35**(6), 2011–2023.
17 Y. Li, X. Liu, X. Yang, H. Lei, Y. Zhang and B. Li, Enhancing Upconversion Fluorescence with a Natural Bio-microlens, *ACS Nano*, 2017, **11**(11), 10672–10680.
18 J. T. Xu, A. Gulzar, P. P. Yang, H. T. Bi, D. Yang, S. L. Gai, F. He, J. Lin, B. G. Xing and D. Y. Jin, Recent advances in near-infrared emitting lanthanide-doped nanoconstructs: Mechanism, design and application for bioimaging, *Coord. Chem. Rev.*, 2019, **381**, 104–134.
19 J. Shi, P. W. Kantoff, R. Wooster and O. C. Farokhzad, Cancer nanomedicine: progress, challenges and opportunities, *Nat. Rev. Cancer*, 2017, **17**(1), 20–37.
20 D. E. Owens 3rd. and N. A. Peppas, Opsonization, biodistribution, and pharmacokinetics of polymeric nanoparticles, *Int. J. Pharm.*, 2006, **307**(1), 93–102.

21 R. Singh, D. Pantarotto, L. Lacerda, G. Pastorin, C. Klumpp, M. Prato, A. Bianco and K. Kostarelos, Tissue biodistribution and blood clearance rates of intravenously administered carbon nanotube radiotracers, *Proc. Natl. Acad. Sci. U. S. A.*, 2006, **103**(9), 3357–3362.

22 B. S. Zolnik, A. González-Fernández, N. Sadrieh and M. A. Dobrovolskaia, Nanoparticles and the immune system, *Endocrinology*, 2010, **151**(2), 458–465.

23 K. Pombo García, K. Zarschler, L. Barbaro, J. A. Barreto, W. O'Malley, L. Spiccia, H. Stephan and B. Graham, Zwitterionic-coated "stealth" nanoparticles for biomedical applications: recent advances in countering biomolecular corona formation and uptake by the mononuclear phagocyte system, *Small*, 2014, **10**(3), 2516–2529.

24 L. Rao, Q. F. Meng, L. L. Bu, B. Cai, Q. Huang, Z. J. Sun, W. F. Zhang, A. Li, S. S. Guo, W. Liu, T. H. Wang and X. Z. Zhao, Erythrocyte Membrane-Coated Upconversion Nanoparticles with Minimal Protein Adsorption for Enhanced Tumor Imaging, *ACS Appl. Mater. Interfaces*, 2017, **9**(3), 2159–2168.

25 C. M. Hu, R. H. Fang and L. Zhang, Erythrocyte-inspired delivery systems, *Adv. Healthcare Mater.*, 2012, **1**(5), 537–547.

26 M. H. Cui, R. X. Liu, Z. Y. Deng, G. L. Ge, Y. Liu and L. M. Xie, Quantitative study of protein coronas on gold nanoparticles with different surface modifications, *Nano Res.*, 2014, **7**, 345.

27 L. Rao, L. L. Bu, J. H. Xu, B. Cai, G. T. Yu, X. Yu, Z. He, Q. Huang, A. Li, S. S. Guo, W. F. Zhang, W. Liu, Z. J. Sun, H. Wang, T. H. Wang and X. Z. Zhao, Red Blood Cell Membrane as a Biomimetic Nanocoating for Prolonged Circulation Time and Reduced Accelerated Blood Clearance, *Small*, 2015, **11**(46), 6225–6236.

28 J. S. Suk, Q. Xu, N. Kim, J. Hanes and L. M. Ensign, PEGylation as a strategy for improving nanoparticle-based drug and gene delivery, *Adv. Drug Delivery Rev.*, 2016, **99**(PtA), 28–51.

29 R. Safavi-Sohi, S. Maghari, M. Raoufi, S. A. Jalali, M. J. Hajipour, A. Ghassempour and M. Mahmoudi, Bypassing Protein Corona Issue on Active Targeting: Zwitterionic Coatings Dictate Specific Interactions of Targeting Moieties and Cell Receptors, *ACS Appl. Mater. Interfaces*, 2016, **8**(35), 22808–22818.

30 S. Schöttler, G. Becker, S. Winzen, T. Steinbach, K. Mohr, K. Landfester, V. Mailänder and F. R. Wurm, Protein adsorption is required for stealth effect of poly(ethyleneglycol)- and poly(phosphoester)-coated nanocarriers, *Nat. Nanotechnol.*, 2016, **11**(4), 372–377.

31 Y. Que, C. Feng, G. Lu and X. Huang, Polymer-Coated Ultrastable and Biofunctionalizable Lanthanide Nanoparticles, *ACS Appl. Mater. Interfaces*, 2017, **9**(17), 14647–14655.

32 R. H. Fang, A. V. Kroll, W. Gao and L. Zhang, Cell Membrane Coating Nanotechnology, *Adv. Mater.*, 2018, **30**(23), e1706759.

33 S. Yan, X. Zeng, Y. Tang, B. F. Liu, Y. Wang and X. Liu, Activating Antitumor Immunity and Antimetastatic Effect Through Polydopamine-Encapsulated Core-Shell Upconversion Nanoparticles, *Adv. Mater.*, 2019, **30**, e1905825.

34 L. Wu, L. Zhang, G. Shi and C. Ni, Zwitterionic pH/redox nanoparticles based on dextran as drug carriers for enhancing tumor intercellular uptake of doxorubicin, *Mater. Sci. Eng., C*, 2016, **61**, 278–285.

35 K. Knop, R. Hoogenboom, D. Fischer and U. S. Schubert, Poly(ethylene glycol) in drug delivery: pros and cons as well as potential alternatives, *Angew. Chem., Int. Ed.*, 2010, **49**(36), 6288–6308.

36 M. J. Haney, N. L. Klyachko, Y. Zhao, R. Gupta, E. G. Plotnikova, Z. He, T. Patel, A. Piroyan, M. Sokolsky, A. V. Kabanov and E. V. Batrakova, Exosomes as drug delivery vehicles for Parkinson's disease therapy, *J. Controlled Release*, 2015, **207**, 18–30.

37 C. Wang, X. Cheng, Y. Sui, X. Luo, G. Jiang, Y. Wang, Z. Huang, Z. She and Y. Deng, A noticeable phenomenon: thiol terminal PEG enhances the immunogenicity of PEGylated emulsions injected intravenously or subcutaneously into rats, *Eur. J. Pharm. Biopharm.*, 2013, **85**(3 PtA), 744–751.

38 A. S. Abu Lila, H. Kiwada and T. Ishida, The accelerated blood clearance (ABC) phenomenon: clinical challenge and approaches to manage, *J. Controlled Release*, 2013, **172**(1), 38–47.

39 R. H. Fang, C. M. Hu, B. T. Luk, W. Gao, J. A. Copp, Y. Tai, D. E. O'Connor and L. Zhang, Cancer cell membrane-coated nanoparticles for anticancer vaccination and drug delivery, *Nano Lett.*, 2014, **14**(4), 2181–2188.

40 C. M. Hu, L. Zhang, S. Aryal, C. Cheung, R. H. Fang and L. Zhang, Erythrocyte membrane-camouflaged polymeric nanoparticles as a biomimetic delivery platform, *Proc. Natl. Acad. Sci. U. S. A.*, 2011, **108**(27), 10980–10985.

41 J. R. Durocher, R. C. Payne and M. E. Conrad, Role of sialic acid in erythrocyte survival, *Blood*, 1975, **45**(1), 11–20.

42 J. R. Peng, Q. Yang, W. T. Li, L. W. Tan, Y. Xiao, L. J. Chen, Y. Hao and Z. Y. Qian, Erythrocyte-membrane-coated Prussian blue/manganese dioxide nanoparticles as H2O2-Responsive oxygen generators to enhance cancer chemotherapy/photothermal therapy, *ACS Appl. Mater. Interfaces*, 2017, **9**(51), 44410–44422.

43 P. A. Oldenborg, A. Zheleznyak, Y. F. Fang, C. F. Lagenaur, H. D. Gresham and F. P. Lindberg, Role of CD47 as a marker of self on red blood cells, *Science*, 2000, **288**(5473), 2051–2054.

44 J. C. Knight and B. Cornelissen, Bioorthogonal chemistry: implications for pretargeted nuclear (PET/SPECT) imaging and therapy, *Am. J. Nucl. Med. Mol. Imaging*, 2014, **4**(2), 96–113.

45 Q. Dai, Y. Yan, C. S. Ang, K. Kempe, M. M. Kamphuis, S. J. Dodds and F. Caruso, Monoclonal antibody-functionalized multilayered particles: targeting cancer cells in the

presence of protein coronas, *ACS Nano*, 2015, **9**(3), 2876–2885.
46 R. H. Fang, C. M. Hu, K. N. Chen, B. T. Luk, C. W. Carpenter, W. Gao, S. Li, D. E. Zhang, W. Lu and L. Zhang, Lipid-insertion enables targeting functionalization of erythrocyte membrane-cloaked nanoparticles, *Nanoscale*, 2013, **5**(19), 8884–8888.
47 R. M. Hochmuth, C. A. Evans, H. C. Wiles and J. T. McCown, Mechanical measurement of red cell membrane thickness, *Science*, 1983, **220**(4592), 101–102.
48 F. Wang and X. Liu, Upconversion multicolor fine-tuning: visible to near-infrared emission from lanthanide-doped NaYF4 nanoparticles, *J. Am. Chem. Soc.*, 2008, **130**(17), 5642–5643.
49 J. Sudimack and R. J. Lee, Targeted drug delivery via the folate receptor, *Adv. Drug Delivery Rev.*, 2000, **41**(2), 147–162.
50 H. S. Krishnan, L. Ma, N. Vasdev and S. H. Liang, (18) F-Labeling of Sensitive Biomolecules for Positron Emission Tomography, *Chemistry*, 2017, **23**(62), 15553–15577.
51 W. Tang, Z. Zhen, M. Wang, H. Wang, Y. J. Chuang, W. Zhang, G. D. Wang, T. Todd, T. Cowger, H. Chen, L. Liu, Z. Li and J. Xie, Red Blood Cell-Facilitated Photodynamic Therapy for Cancer Treatment, *Adv. Funct. Mater.*, 2016, **26**, 1757–1768.
52 H. Jick, D. Slone, B. Westerholm, W. H. Inman, M. P. Vessey, S. Shapiro, G. P. Lewis and J. Worcester, Venous thromboembolic disease and ABO blood type, A cooperative study, *Lancet*, 1969, **1**(7594), 539–542.